Fluctuation characteristics and transport properties of collisionless trapped electron mode turbulence

Yong Xiao,[1] Ihor Holod,[1] Wenlu Zhang,[1] Scott Klasky,[2] and Zhihong Lin[1]
[1]*Department of Physics and Astronomy, University of California, Irvine, California 92697, USA*
[2]*Oak Ridge National Laboratory, Oak Ridge, Tennessee 37831, USA*

(Received 27 August 2009; accepted 4 January 2010; published online 12 February 2010)

The collisionless trapped electron mode turbulence is investigated by global gyrokinetic particle simulation. The zonal flow dominated by low frequency and short wavelength acts as a very important saturation mechanism. The turbulent eddies are mostly microscopic, but with a significant portion in the mesoscale. The ion heat transport is found to be diffusive and follows the local radial profile of the turbulence intensity. However, the electron heat transport demonstrates some nondiffusive features and only follows the global profile of the turbulence intensity. The nondiffusive features of the electron heat transport is further confirmed by nonlognormal statistics of the flux-surface-averaged electron heat flux. The radial and time correlation functions are calculated to obtain the radial correlation length and autocorrelation time. Characteristic time scale analysis shows that the zonal flow shearing time and eddy turnover time are very close to the effective decorrelation time, which suggests that the trapped electrons move with the fluid eddies. The fluidlike behaviors of the trapped electrons and the persistence of the mesoscale eddies contribute to the transition of the electron turbulent transport from gyro-Bohm scaling to Bohm scaling when the device size decreases. © *2010 American Institute of Physics*.
[doi:10.1063/1.3302504]

I. INTRODUCTION

Anomalous transport in tokamak plasma is generally believed due to the microturbulence excited by drift wave instabilities.[1] At present the ion turbulent transport driven by ion temperature gradient (ITG) turbulence becomes relatively clear after intensive research of the last several decades. For example, in the ITG turbulence, the zonal flow shearing is found to regulate the ion heat transport by breaking the radial streamers[2–5] and the ion transport scaling has been found to change from the Bohm to the gyro-Bohm when the device size increases.[6] However, the electron turbulent transport is much less understood. The electron transport is becoming an important issue in the burning plasmas, such as ITER,[7] because the energetic fusion products (α-particles) will mostly heat the electrons. As a prominent candidate for the electron transport, the collisionless trapped electron mode (CTEM) has gained a renewed interest with the advance of gyrokinetic simulation. Driven by the magnetically trapped electrons,[8] the CTEM instability has two types of excitation mechanisms in the collisionless limit: the kinetic instability driven by the toroidal precessional resonance between the trapped electrons and the electrostatic drift waves,[9] and the reactive fluid instability driven by the electron magnetic drift when the instability drive is very strong.[10]

In the late 1970s, the linear CTEM instability was extensively studied by the analytic theory,[11,12] when only very limited attention was paid to the nonlinear physics of the CTEM turbulence[13] due to its extreme complexity. Later, some nonlinear theory began to deal with this complexity.[14,15] With the advance of the gyrokinetic theory[16–18] and numerical algorithm,[19–23] as well as the fast-increasing computational power, the massively parallel gyrokinetic simulations have emerged as a major tool to investigate the nonlinear physics of the microturbulence. Here we apply the gyrokinetic toroidal code (GTC) (Ref. 2) to study the CTEM turbulence physics, particularly, nonlinear saturation mechanism and transport mechanism.

The zonal flow shearing has been discovered in the ITG turbulence as the dominant saturation mechanism.[2,24–26] However, its role in the CTEM turbulence has been an ongoing debate between different gyrokinetic simulations, either particle or continuum.[27–30] For example, the zonal flow shearing rates between two gyrokinetic codes do not agree with each other for $\eta_e > 3$, at least quantitatively. The findings of these two codes,[29,30] that the zonal flow is not important for $T_e > 3T_i$, may not be relevant since most tokamak experiments operate at $T_e \sim T_i$. However, even this agreement is soon challenged.[31] Therefore, until a clear physics picture is provided, such as that for the ITG turbulence,[25,26] the effect of zonal flow in the CTEM turbulence remains an open issue. In our simulation, the zonal flow is still very important in saturating the CTEM turbulence. The temporal and spatial structures of the zonal flow are then carefully examined in our study. It is found that the low frequency zonal flow dominates the frequency spectrum.

To understand the transport mechanism it is important to examine the detailed turbulence properties, such as wave spectrum, frequency spectrum, correlation length and correlation time.[32] These detailed properties can provide important information to validate the simulation with experiments,[33,31] as well. We calculated two-point correlation function and two-time-two-point correlation function[34] for the CTEM turbulence. These two-dimensional (2D) correla-

 © 2010 American Institute of Physics

tion functions are used to calculate the radial correlation length, turbulence autocorrelation time and toroidal wave propagation speed. The radial correlation length of the turbulence eddies has a two-scale structure: a microscopic length of several ion gyroradii and a mesoscale length of several tens of ion gyroradii. This two-scale structure persists for different device sizes. The mesoscale eddies are formed in a competing process between the breaking of the macroscopic streamers by the zonal flow and the merging of the microscopic eddies.[35]

The electron heat transport in the CTEM turbulence exhibits some nondiffusive features and smooths out the local radial profile of the turbulence intensity that the ion heat transport closely tracks. Our statistical analysis support the nondiffusive feature of the electron heat flux. A comprehensive set of characteristic time scales is calculated to investigate the transport mechanism. The fluid time scales, especially the zonal flow shearing time τ_s and the eddy turnover time τ_{eddy}, are found to be very close to the effective decorrelation time. This confirms the importance of the zonal flow in the turbulence saturation process. All the kinetic time scales are much longer than the fluid time scales. Therefore, the trapped electrons in the CTEM turbulence are believed to move with the turbulence eddies as fluid elements. As a comparison, the characteristic time analysis for the ions in the ITG turbulence with adiabatic electrons shows that the parallel wave-particle decorrelation is the dominant transport mechanism for the ITG turbulence. Therefore, the electron transport in the CTEM turbulence is a one-dimensional (1D) (radial) process, while the ion transport is a 2D (parallel +radial) process.

The resonant trapped electrons can move ballistically in the mesoscale eddies, which leads to a nondiffusive component in the electron heat flux. The ballistic electron heat flux may be responsible for the experimental observations of the residual electron transport inside the internal transport barrier (ITB), where the ion transport is mostly neoclassical.[36] The persistence of the mesoscale eddies in the CTEM turbulence for different device sizes, together with the possible turbulence spreading effects,[32] leads to the observed transition of the electron transport scaling from gyro-Bohm to Bohm when the device size decreases.[35]

II. NONLINEAR SATURATION

In this section, we introduce the physical parameters applied in the simulation and study the heat transport, as well as the nonlinear saturation mechanism of the CTEM instability.

A. Physical parameters

The GTC code is a well-benchmarked gyrokinetic particle simulation code for studying microturbulence in tokamaks.[2] The code applies a global field-aligned mesh that change the computation scaling on device size from $(a/\rho_i)^3$ to $(a/\rho_i)^2$ and reduces the number of toroidal grids to 100 times fewer, where a is the tokamak minor radius and ρ_i is the ion gyroradius. For the ions, the GTC code solves the gyrokinetic equation, where the gyroaverage is implemented by the four point or eight point average in the real configuration space.[19,37] For the electrons, the GTC code employs the drift kinetic equation because of the small electron gyroradius. Since the electrons move $\sqrt{m_i/m_e}$ times faster than the ions, where m_i is the ion mass and m_e is the electron mass, a much smaller time step is required to satisfy the parallel *Courant* condition and solve the kinetic electron motion accurately. Apparently this brute force method is computationally challenging. Instead, the GTC code employs a electrostatic fluid-kinetic hybrid model for the electrons in the CTEM simulation.[38,39] In this model, the electrostatic potential is decomposed into a zonal part and a nonzonal part, $\tilde{\phi}=\langle\phi\rangle+\delta\phi$. Based on the fact that the electron's response to the zonal part $\langle\phi\rangle$ is negligible[40] and the response to the nonzonal part $\delta\phi$ is mainly adiabatic for passing electrons,[9] we can expand the electron drift kinetic equation using the smallness parameter, $\sqrt{m_e/m_i}$. As a matter of fact, we always keep the realistic mass ratio in the simulation, whereas most other gyrokinetic simulation codes have to use the reduced mass ratio to relieve the computational burden. The GTC code uses the Adaptable I/O System,[41] ADIOS, to provide ultrafast parallel file I/O support for the large data in the turbulence fluctuation analysis. The GTC code has been successfully benchmarked with other simulation codes including the FULL code and the GT3D code on the linear CTEM instability.[42]

For the nonlinear simulation of the CTEM turbulence, we employ the following typical DIII-D parameters: $R_0/L_{Te}=6.9$, $R_0/L_{Ti}=2.2$, $R_0/L_n=2.2$, $T_e/T_i=1$, $m_i/m_e=1837$, $q=0.58+1.09r/a+1.09(r/a)^2$, with $q=1.4$ and $s\equiv(r/q)(dq/dr)=0.78$ at $r=0.5a$. The circular cross section model is used in the simulation for the equilibrium magnetic field. The simulation is carried out in an annulus between $0.1a$ and $0.9a$. From the linear benchmark,[42] we learned that with this set of parameters the CTEM is the only electrostatic instability on the ρ_i scale. The field mesh in the simulation consists of 32 toroidal grids and a unstructured perpendicular mesh with the perpendicular grid size $\sim 0.5\rho_i$ to capture the short wavelength mode of the CTEM turbulence. According to the linear simulation,[42] we note that this set of parameters falls in the category of the kinetic CTEM instability,[9] mainly driven by the toroidal precessional resonance. In addition, as a comparison we carried out a simulation for the ITG turbulence by increasing the ion temperature gradient, which represents ITG driven turbulence with adiabatic electrons. For this ITG case the ITG is increased to $R_0/L_{Ti}=6.9$, while keeping other parameters the same as the CTEM case. The ions in the ITG turbulence are the proactive species that drives the instability, which can be used to compare to the active species in CTEM, i.e., the trapped electrons. The default system size in this paper is set as $a/\rho_i=500$.

In the current GTC code, the δf method is used to reduce the numerical noise with the one particle distribution function $f=F_0+\delta f$ and F_0 is set as a local *Maxwellian* in the simulation.[20] However, the numerical particle noise intrinsically associated with the δf algorithm cannot be completely annihilated.[43] It has been known that the noise driven transport increases with the entropy of the system, i.e., the sum of

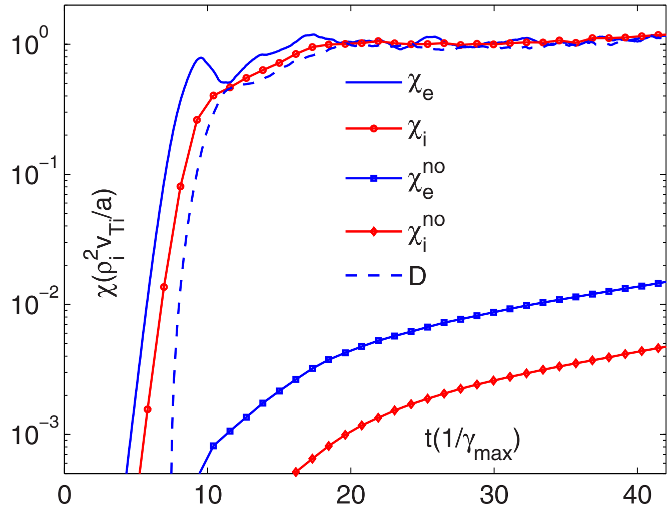

FIG. 1. (Color online) Time history of electron heat conductivity χ_e (solid line), ion heat conductivity χ_i (circle), particle diffusivity(dashed line), and noise induced transport (square for electrons and diamond for ions) in the nonlinear CTEM simulation, where $\gamma_{\max}$ represents the maximum linear growth rate.

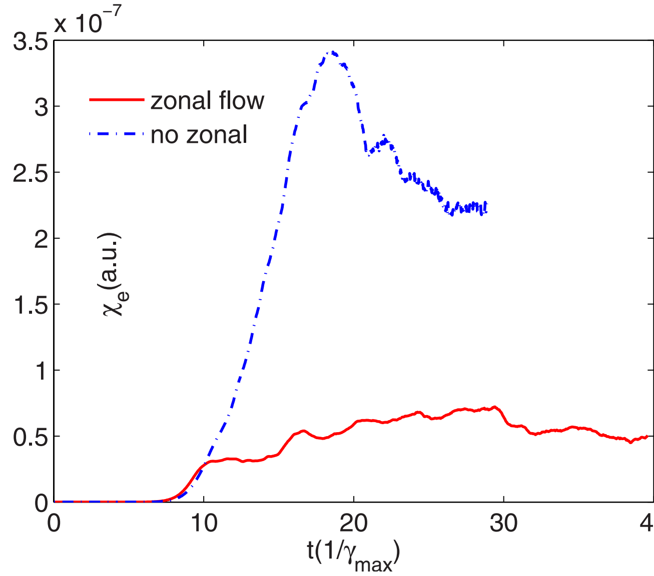

FIG. 2. (Color online) The time history of heat transport for $a/\rho_i=250$. The solid line has the zonal flow self-consistently generated, while the dotted line has the zonal flow artificially removed.

the square of particle weights.[44,45] Hence, the noise driven transport can be estimated as $\chi_N(t)=\chi_N(0)\langle w^2(t)\rangle/\langle w^2(0)\rangle$, where $\chi_N(t)$ is the noise driven heat conductivity at time t and $w(t)=\delta f(t)/f$ is the particle weight and $\langle w^2(t)\rangle$ is the ensemble average of $w^2(t)$, which represents the entropy of the system. As shown in Fig. 1, the noise driven heat transport is only around 1% of the total transport for both the electrons and ions after the nonlinear saturation by using 100 particles per cell. Therefore, by setting sufficient number of particles per cell, the particle noise cannot affect the physics results significantly and is no longer a major concern for our CTEM simulation. In the simulation, the heat conductivity χ_j is defined through $q_j=n_j\chi_j\nabla T_j$, $j=i,e$. Note the current definition of χ_e is traditional and different from our earlier definition in Ref. 35, where the trapped electron density is used to calculate the time scale of the heat transport, which mainly comes from the trapped electrons. The heat flux q_j is calculated in the simulation by $q_j=\int d^3v\left(\frac{1}{2}v^2-\frac{3}{2}T_j\right)\delta v_r\delta f_j$, where v is the particle velocity, δv_r is the radial component of the gyroaveraged $E\times B$ drift, and δf_j is the perturbed distribution function. The temperature T_j is related to thermal speed v_j by $v_j=\sqrt{T_j/m_j}$ and the gyroradius $\rho_j=v_j/\Omega_j$ with $\Omega_j=e_jB_j/m_jc$ the gyrofrequency.

B. Zonal flow regulation

As shown in Fig. 1, in the CTEM simulation, the particles are initially randomly distributed and produces no heat transport; then the heat transport begins to grow exponentially due to the linear instability caused by the toroidal precessional resonance; finally the heat transport saturates and reaches a stochastic equilibrium. It is known that zonal flow, the axisymmetric $E\times B$ flow, excited by microturbulence through nonlinear mode coupling, are the dominant saturation mechanism in the ITG turbulence.[2] The simulation extends over several tens of maximum growth time, which is much longer than the characteristic time scale of the physics we are studying, the nonlinear physics that leads to the turbulence transport. To evaluate the zonal flow effect in the CTEM turbulence, here we compare the two simulation cases, one with the zonal flow self-consistently generated and the other one with zonal flow artificially removed, as shown in Fig. 2. The CTEM turbulence saturation level without zonal flow is shown to be much higher than the one with zonal flow. This clearly shows that zonal flow are very important in saturating the CTEM turbulence for the simulation parameters. The formation of macroscopic size eddies or streamers leads to the higher transport level in the case without the zonal flow regulation. With the zonal flow regulation, the streamers are broken into mostly small isotropic eddies and a significant portion of mesoscale eddies, which substantially reduces the transport level.[35] The result, that the zonal flow is important in regulating the CTEM turbulence, is actually consistent with the existing literature for the parameter regime studied. In Fig. 2, we compare two cases of device size $a/\rho_i=250$ to relieve the computational burden without significantly influencing the zonal flow physics.

The time-radial 2D structure of the zonal flow potential is shown in Fig. 3. After nonlinear saturation $[t>10/\gamma_{\max}$ with $\gamma_{\max}=0.25L_{ne}/v_i$ (Ref. 42)], the zonal flow potential has a strong short wavelength component with $\langle k_r\rho_i\rangle\sim 0.7$, as shown in the upper panel of Fig. 4, since the short wavelength zonal flow are not easily screened by the neoclassical effects.[46–49] The lower panel of Fig. 4 shows the radial wave spectrum at a typical time moment after saturation. To calculate $\langle k_r\rho_i\rangle$ from the lower panel, we exclude those very long wavelengths that usually represents mean flow, since these zonal flows have very weak shearing effect[50] and whether they are treated in a sufficiently satisfactory way is a topic of current interest.[51–53] There is a downshift of zonal flow wavelength during the nonlinear saturation. This downshift is caused by the downshift of the perpendicular spectrum of the drift wave turbulence in Fig. 6(a), which is ex-

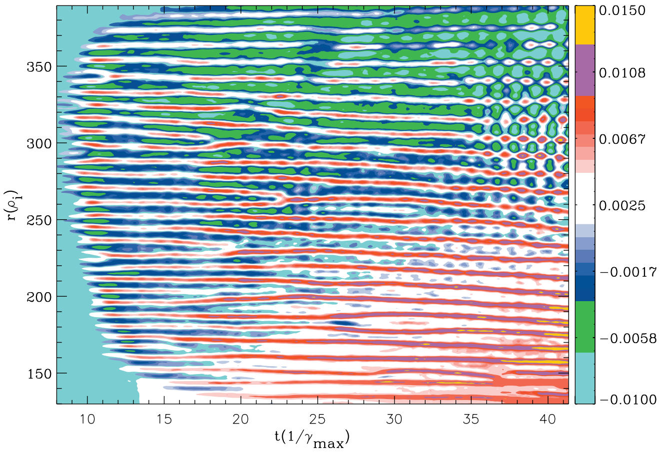

FIG. 3. (Color) Zonal flow structures in both time and radial directions.

cited by the linear CTEM instability and believed to be the energy source of the zonal flow.[25,26] Fixing on one radial location $r>0.5a$ in Fig. 3, we can see that the zonal flow varies with time. This time oscillation of zonal flow is the geodesic acoustic mode (GAM). For each radial location, the frequency response of the zonal flow can be calculated and then the GAM frequency spectrum can be averaged over different radii. The average GAM frequency is found to be $\omega_{GAM}\approx 2.6v_i/R_0$, which is very close to the theoretical value $2.68v_i/R_0$ from the formula[54,55]

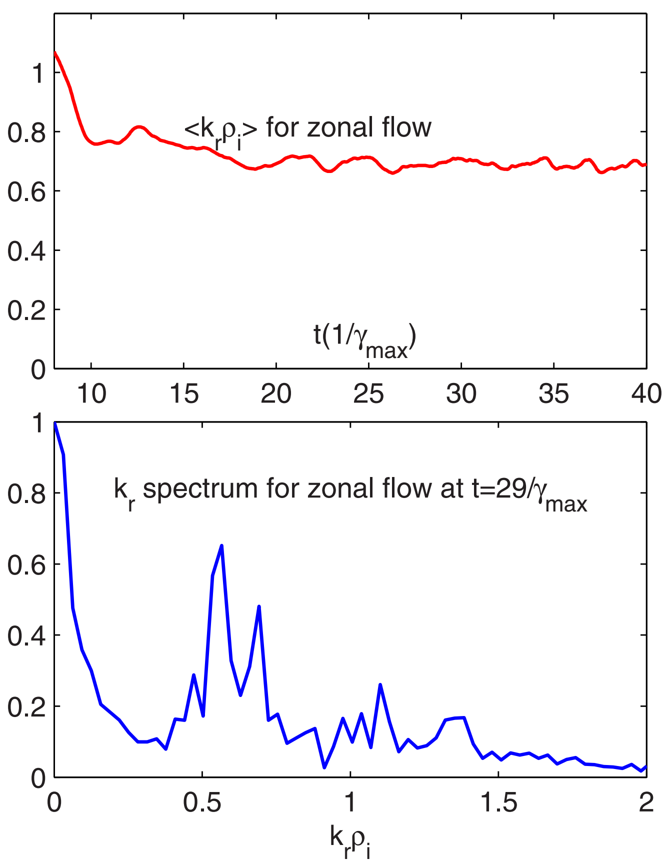

FIG. 4. (Color online) Upper panel shows the time history of the average radial wave vector of the zonal flow. Lower panel shows that radial wave vector spectrum of the zonal flow at $t=29/\gamma_{max}$.

TABLE I. Characteristic time scales for trapped electrons in the CTEM turbulences and for ions in the ITG turbulence.

$[L_{ne}/v_i]$	τ_{decor}	$\tau_{\parallel}$	$\tau_{\perp}$	τ_{eddy}	τ_{au}	τ_s	$1/\gamma_{max}$
CTEM e	0.61	∞	∞	1.6	11	0.66	4.0
ITG i	1.7	1.8	2.0	4.9	7.2	1.4	9.1

$$\omega_{GAM} = \sqrt{\frac{2}{m_i}\left[T_e + \frac{7}{4}T_i\left(1+\frac{46}{49q^2}\right)\right]} \Bigg/ R_0.$$

The GAM frequency is higher than the turbulence autocorrelation frequency $\omega_{au}\approx 2\pi/\tau_{au}\approx 1.3v_i/R_0$, which can be found in Table I. This indicates that the GAM mode could only have a weak regulation effect on the CTEM turbulence. Since the low frequency dominates the zonal flow spectrum, as shown in Fig. 3, it is still the low frequency zonal flow rather than the GAM that mainly regulates the CTEM turbulence. The GAM oscillation is stronger in the outside of the radial domain where the linear damping of GAM is weaker due to the larger q value since that the linear GAM damping rate γ_{GAM} decreases with the safety factor q, i.e., $\gamma_{GAM}\sim q^5\exp(-7q^2/4)$.[54,56] In addition, the GAM oscillation occurs after the zonal flow is excited. This indicates that first the turbulence excites the zonal flow and then the zonal flow excites the GAM mode by a geodesic energy transfer process.[57]

III. TURBULENCE CHARACTERISTICS

In this section, we proceed to discuss the characteristics of the CTEM turbulence and compare it with that of the ITG turbulence. In the GTC simulation, the $3D(r,\theta,\zeta)$ turbulence data is recorded at each time step for further quantitative analysis.

A. Ballooning structure

In a tokamak, the particles feel larger magnetic drift (∇B and curvature drift) in the outer side ($\theta=0$) on each flux surface than the inner side ($\theta=\pi$). The anisotropy of the magnetic drift effect within a bounce period leads to a universal ballooning mode structure of the turbulence fluctuations.[58] Our simulation is able to demonstrate this ballooning feature, as a verification of the global code. The turbulence potential on the $r=0.5a$ flux surface, plotted in Fig. 5, shows a typical (α,ζ) 2D turbulence structure at the nonlinear stage, where ζ is the toroidal angle and $\alpha=\theta-\zeta/q$ is the field line label. In this figure the turbulence fluctuations are elongated along each field line, one of the key features of the microturbulence in a magnetized plasma. Moreover, the maximum potential point on each field line forms a straight line with slope approximately $-1/q$. By transforming the field-aligned coordinate (α,ζ) to the magnetic coordinates (θ,ζ), this feature actually shows that the turbulence should have a maximum value at the poloidal angle $\theta=0$. We can define a flux-surface-averaged parallel angle $\langle\theta^2\rangle=\langle\int_{-\pi}^{\pi}d\theta|\delta\phi|^2\theta^2/\int_{-\pi}^{\pi}d\theta|\delta\phi|^2\rangle$ by integrating along each field line, which represents the mean parallel wave-

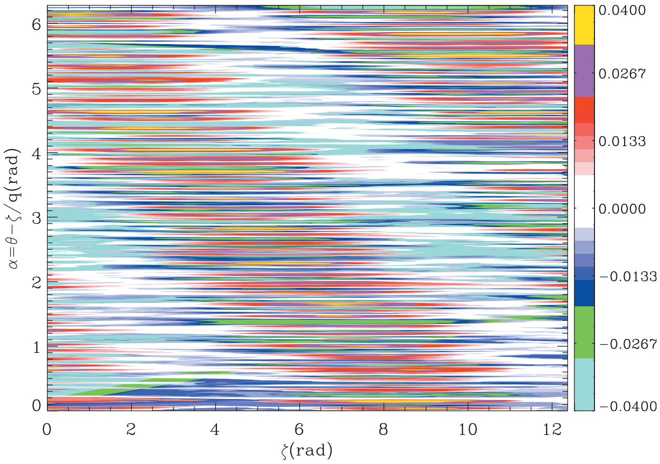

FIG. 5. (Color) The contour plot of the electrostatic potential $\delta\phi$ on a flux surface at $t=29/\gamma_{\max}$ for $r=0.5a$ with ζ the toroidal angle and α the field line variable.

length. For a more precise representation of the parallel angle, we shall consider the statistical fluctuation of $\langle\theta^2\rangle$ in the nonlinear stage, i.e., averaging $\langle\theta^2\rangle$ over many time steps. The time averaged parallel angle is found to be $\langle\theta^2\rangle=1.14$ for the CTEM turbulence and $\langle\theta^2\rangle=2.54$ for the ITG turbulence. So the CTEM turbulence has a smaller mean parallel angle than the ITG turbulence, which suggests that the kinetic electron response reduces the mean parallel angle $\langle\theta^2\rangle$, i.e., the CTEM turbulence forms a stronger ballooning structure, and the mode coupling between neighboring poloidal harmonics is tighter in the CTEM turbulence. This is essentially a feature of the linear instability.[42] With the mean parallel angle $\langle\theta^2\rangle$, we can calculate the mean radial wavelength $\sqrt{\langle k_r^2\rangle}=s^2\langle\theta^2\rangle\sqrt{\langle k_\theta^2\rangle}$, where s is the magnetic shear defined as $s=d\ln q/d\ln r$. This value of $\sqrt{\langle k_r^2\rangle}$ is actually the range of radial wavelengths that one particle could see within a bounce motion, and will be used to calculate the particle diffusion time among different poloidal harmonics.[34]

B. Turbulence spectrum evolution

The $3D$+time turbulence data can also be used to calculate the parallel and perpendicular spectrum, e.g., $\langle k_\parallel\rangle=\Sigma_k|\delta\phi_k|^2|k_\parallel|/\Sigma_k|\delta\phi_k|^2$, $\Delta k_\parallel=\sqrt{\langle k_\parallel-\langle k_\parallel\rangle\rangle^2}$, $\langle k_\perp^2\rangle=\Sigma_k|\delta\phi_k|^2|k_\theta|/\Sigma_k|\delta\phi_k|^2$, and $\Delta k_\perp=\sqrt{\langle k_\perp-\langle k_\perp\rangle\rangle^2}$, as shown in Fig. 6. In the linear stage ($t<8/\gamma_{\max}$), the perpendicular spectrum of the CTEM mode has a shorter wavelength than that of the ITG turbulence because the short wavelength modes have a larger linear growth rate than the long wavelength modes.[42] Then the radial spectrum of zonal flow is shifted to the short wavelength regime by the mode-mode coupling of the ambient short wavelength turbulence ($8/\gamma_{\max}<t<9/\gamma_{\max}$), as seen in Fig. 4. Later during the nonlinear saturation, the perpendicular spectrum of the CTEM turbulence shifts to the longer wavelength,[29] so does the zonal flow. However, the parallel spectrum of the CTEM turbulence keeps roughly constant in this transition. While in the ITG case, the perpendicular spectrum downshifts slightly and the parallel spectrum upshifts slightly toward the shorter

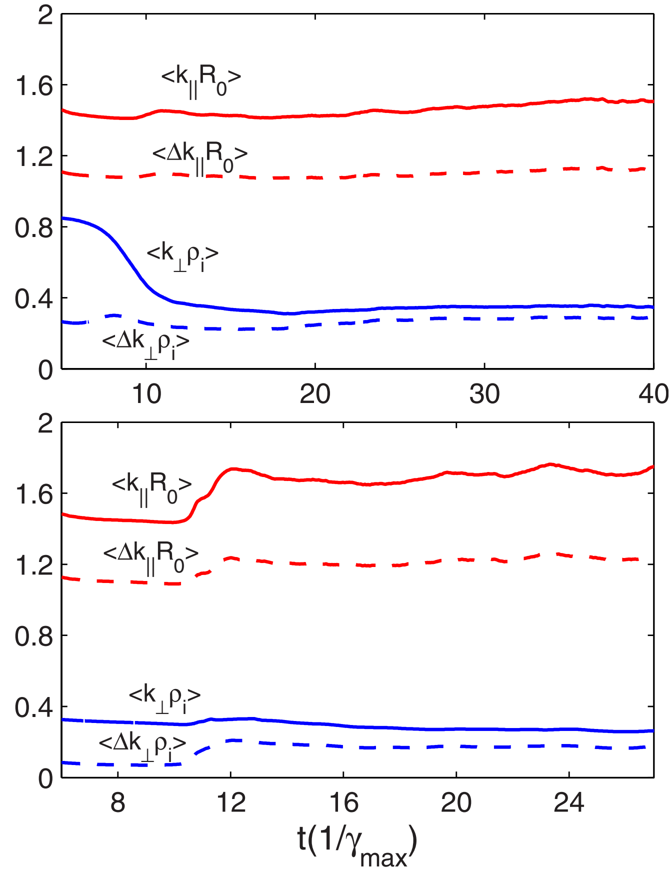

FIG. 6. (Color online) Time history of the average parallel and perpendicular wave vector and their respective spectrum width for CTEM turbulence in the upper panel (a) and ITG(a) turbulence in the lower panel (b).

wavelength, as shown in Fig. 6. Therefore, the spectrum evolution indicates that the CTEM turbulence is more related to the perpendicular wave-particle dynamics, while ITG turbulence is more related to the parallel wave-particle dynamics. This will be further confirmed by our detailed time scale analysis.

C. Radial correlation length

The radial correlation length is an important measure of the turbulence structure, which can be clearly seen by the radial-toroidal 2D turbulence contour from the CTEM simulation in Fig. 7. This figure is dominated by turbulence eddies with radial length of several ρ_i. From the data in Fig. 7, we can calculate the two-point correlation function,

$$C_{r\zeta}(\Delta r,\Delta\zeta)=\frac{\langle\delta\phi(r+\Delta r,\zeta+\Delta\zeta)\delta\phi(r,\zeta)\rangle}{\sqrt{\langle\delta\phi^2(r+\Delta r,\zeta+\Delta\zeta)\rangle\langle\delta\phi^2(r,\zeta)\rangle}}. \quad (1)$$

Then for each Δr, the maximum of $C_{r\zeta}(\Delta r,\Delta\zeta)$ can be calculated to give the radial correlation function $C_r(\Delta r)$ for different device sizes, as shown in Fig. 8. Note that all these correlation curves are calculated from the data at one time step. So there are some statistical fluctuations, especially for the mesoscale structures of the $a/\rho_i=125$ case. These radial correlation functions all drops exponentially for the small radial separation with a characteristic length of $5\rho_i$, which fits the exponential decay model $\exp(-\Delta r/L_r)$ and the radial

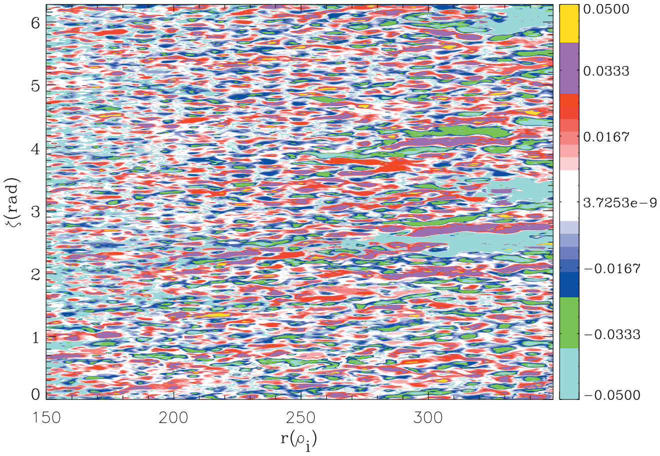

FIG. 7. (Color) The contour plot of the electrostatic potential $\delta\phi$ on the (r,ζ) plane at $t=29/\gamma_{\max}$ for the poloidal angle $\theta=0$.

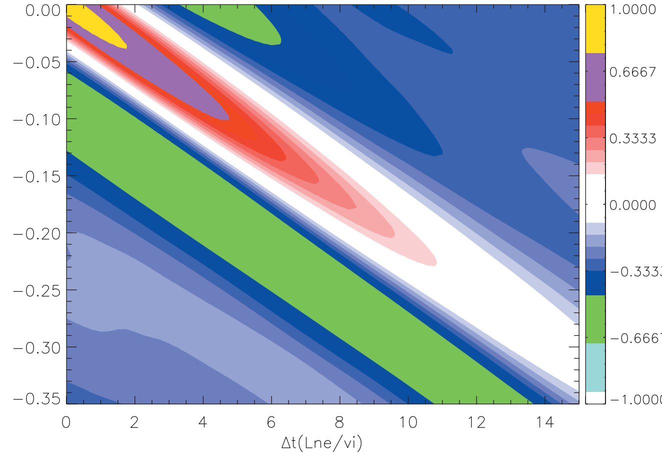

FIG. 9. (Color) Contour plot for the two-time-two-point correlation function $C_{t\zeta}(\Delta t,\Delta\zeta)$ of the electronstatic potential $\delta\phi$, in which the unit of $\Delta\zeta$ is radian.

correlation length L_r represents the microscopic eddy size. In addition, there is a significant tail in the correlation function, notably persisting for all device sizes, which represents the mesoscale eddies of several tens of ρ_i. On the contrary, there exist mostly microscopic eddies in the ITG turbulence for different device sizes.[32] To reduce the statistical error, the radial correlation length can be time-averaged over multiple time steps to obtain the mean microscopic eddy size, $L_r=5.6\rho_i$ for the CTEM turbulence. As a comparison, we find $L_r=8.0\rho_i$ for the ITG turbulence. So the mean microscopic eddy size in the CTEM turbulence is shorter than that in ITG.

D. Wave propagation and autocorrelation time

An important characteristic time for the turbulence is the autocorrelation time $\tau_{\rm au}$, which describes how long the turbulence eddy can exist. In order to calculate $\tau_{\rm au}$, the two-time-two-point correlation function $C_{t\zeta}(\Delta t,\Delta\zeta)$ defined by

$$C_{t\zeta}(\Delta t,\Delta\zeta)=\frac{\langle\delta\phi(t+\Delta t,\zeta+\Delta\zeta)\delta\phi(t,\zeta)\rangle}{\sqrt{\langle\delta\phi^2(t+\Delta t,\zeta+\Delta\zeta)\rangle\langle\delta\phi^2(t,\zeta)\rangle}},\tag{2}$$

needs to be computed. From the turbulence data, the potential value at line ($\theta=0$, $r=0.5a$) can be extracted at each time step to obtain a 2D potential data $\phi(t,\zeta)$. The two-time-two-point correlation function $C_{t\zeta}(\Delta t,\Delta\zeta)$ can then be generated, as shown in Fig. 9. In this figure, the CTEM turbulence propagates in the electron diamagnetic direction ($-\zeta$). This direction is counter to the direction of the ITG turbulence propagation, which is in the ion diamagnetic direction ($+\zeta$). From Fig. 9, the toroidal phase velocity for the CTEM turbulence can be calculated by $\dot{\zeta}=0.02v_i/L_n$, which is the toroidal precession frequency.

Following the maxima ridge in Fig. 9, the time correlation function $C_t(\Delta t)$ can be obtained. The exponential decay model $\exp(-\Delta t/\tau_{\rm au})$ is found to very well suit the correlation

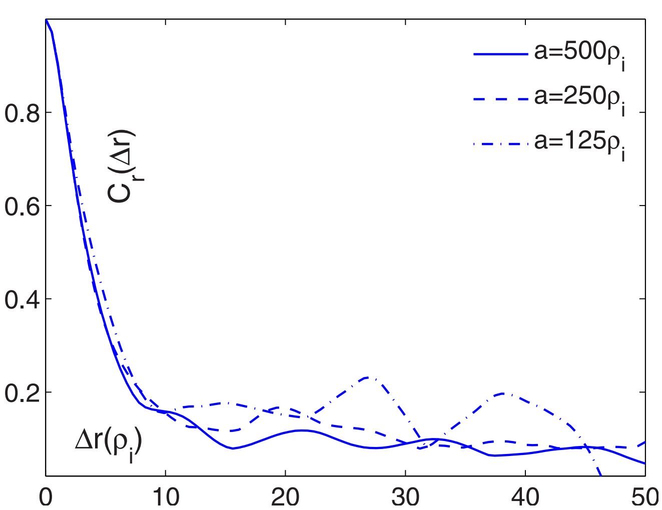

FIG. 8. (Color online) Radial correlation function $C_r(\Delta r)$ of the electrostatic potential $\delta\phi$ for different device sizes.

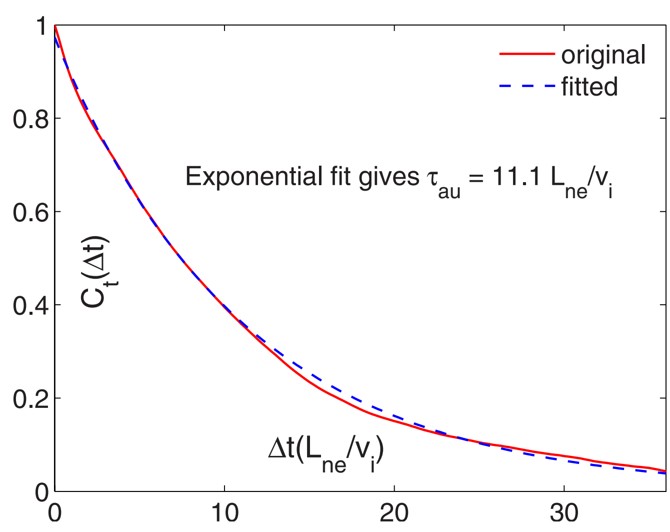

FIG. 10. (Color online) Time correlation function $C_t(\Delta t)$ of the electrostatic potential $\delta\phi$ and its exponential fit, which gives the autocorrelation time $\tau_{\rm au}=11.1L_{Ti}/v_{Ti}$.

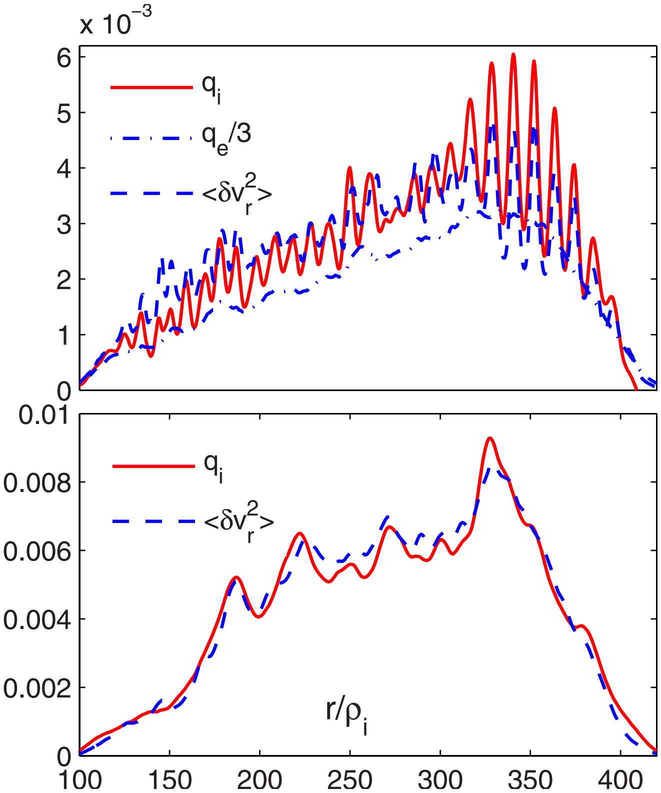

FIG. 11. (Color online) Radial profile of the heat flux q_i, q_e and the $E\times B$ drift intensity $\langle \delta v_r^2 \rangle$ for a/ρ_i=500 with the upper panel (a) for the CTEM turbulence and lower panel (b) for the ITG(a) turbulence.

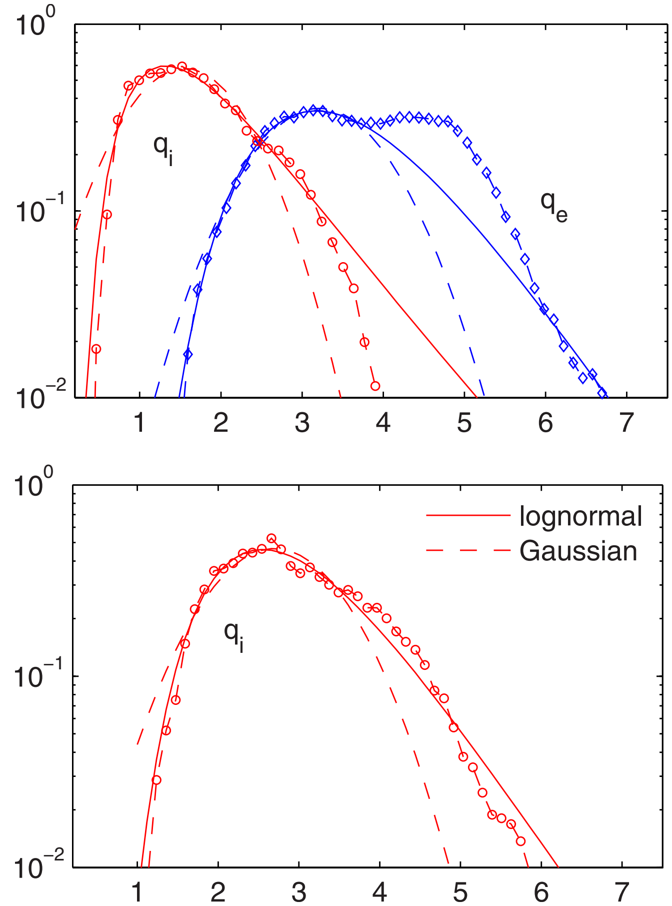

FIG. 12. (Color online) The probability density function (PDF) of the flux-surface-averaged electron heat flux q_e and ion heat flux q_i in the CTEM turbulence, shown in the upper panel (a), and ion heat flux q_i in the ITG turbulence, shown in the lower panel (b) with the electron heat flux normalized by $n_{tr}\nabla T_e$ and ion heat flux normalized by $n_0\nabla T_i$, where n_{tr} is the trapped electron density. The solid line is a lognormal distribution fit and the dashed line is a Gaussian distribution fit.

function $C_t(\Delta t)$, as shown in Fig. 10, which gives the autocorrelation time $\tau_{au}=11.1 L_{Ti}/v_i$ for the CTEM turbulence.

IV. NONLINEAR HEAT TRANSPORT MECHANISM

After exploring all the requisite turbulence characteristics, we proceed to investigate the nonlinear heat transport mechanism for the CTEM turbulence.

A. Features of CTEM transport

It is of great interest to investigate the electron heat transport mechanism because recent researches indicate that the CTEM turbulence can be a prominent candidate for the electron heat loss in a tokamak.[33,59,60] In the ITG turbulence, the ion heat transport can be described by a quasilinear diffusion model.[61,62] An important consequence of the quasilinear diffusion model is that the local heat conductivity $\chi(r)$ is proportional to the local $E\times B$ drift intensity $\langle \delta v_r^2(r) \rangle$ with $\langle\ \rangle$ denoting flux-surface average. For example, in the ITG turbulence, our simulation finds that the local heat conductivity $\chi_i(r)$ is indeed proportional to $\langle \delta v_r^2(r) \rangle$ for a simulation with device size a/ρ_i=500, as shown in Fig. 11(b). For the CTEM turbulence, the local ion heat conductivity $\chi_i(r)$ is still proportional to $\langle \delta v_r^2(r) \rangle$, as shown in Fig. 11(a), which suggests that the ion heat transport is still driven by the local $E\times B$ drift intensity and the quasilinear diffusion model is suitable for the ion heat transport in the CTEM turbulence. However, from Fig. 11(a), the electron heat conductivity only tracks the global profile of the turbulence intensity $\langle \delta v_r^2(r) \rangle$ and smooths out its local oscillatory feature. This suggests that the electron heat transport follows a transport mechanism different from that in the ion heat transport. The electron heat transport in the CTEM turbulence can contain a nondiffusive component so that quasilinear diffusion model is insufficient to describe the electron dynamics. In addition, the 2D radial-time contour of the electron heat flux in Fig. 3(c) of Ref. 35 shows that the electron heat flux has a radial ballistic propagation which may comes from this nondiffusive component.

The nondiffusive feature of the electron heat transport can be further confirmed by the probability distribution function (PDF) of the flux-surface-averaged electron heat flux, as shown by the circles in Fig. 12(a). If the heat transport is purely a diffusive process, the flux-surface-averaged heat flux should follow the lognormal distribution,[63] which is true for the ion heat fluxes and small electron heat fluxes in Fig. 12(a). However, neither lognormal nor Gaussian distribution can fit well the simulation PDF in the whole range of the electron heat flux. There is a significant large heat flux component that is above the lognormal distribution, which indicates a nondiffusive/superdiffusive component. The large ion heat fluxes are below the lognormal distribution, which may indicate a subdiffusive component. On the contrary, the PDF of the flux-surface-averaged ion heat flux in the ITG turbulence is consistent with the lognormal distribution, as shown in Fig. 12(b), which suggests that the ion heat transport in the ITG turbulence is a diffusive process.[32] The PDF is calculated over a time window of $50L_{ne}/v_i$ for the electron heat flux in the CTEM turbulence and a time window of $100L_{ne}/v_i$ for the ion heat flux in the ITG turbulence, respectively. As shown in Sec. IV B, these time windows are much larger than all the known characteristic time scales, especially the effective decorrelation time, in their respective type of turbulence.

B. Characteristic time scales

Although the electron transport in the CTEM turbulence does not follow the local structure of the turbulence intensity, it still follows the global profile of the turbulence intensity, as shown in Fig. 11(a). This global proportionality enables us to define an effective decorrelation time $\tau_{\rm decor}=2D/\langle \delta v_r^2\rangle$ and a test particle diffusivity D can be related to the electron thermal conductivity χ_e by $D=2\chi_e/3$. From Fig. 11(a), $\sqrt{\langle \delta v_r^2\rangle}=4.7\times 10^{-3}v_i$. It is then calculated that $\tau_{\rm decor}=4\chi_e/(3\langle \delta v_r\rangle^2)\approx 0.61L_n/v_i$ for the trapped electrons. Similarly, $\tau_{\rm decor}=1.7L_n/v_i$ for the ions in the ITG turbulence. This characteristic time scale may reflect the physical process relevant to the transport mechanism,[34] which could be either kinetic wave-particle decorrelation or fluid eddy mixing. Through the following comprehensive analysis of the kinetic and fluid time scales, we can identify the physical process responsible for the transport.

The two kinetic time scales related to the CTEM eigenmodes are the parallel and perpendicular wave-particle decorrelation time ($\tau_\parallel$ and $\tau_\perp$) for the trapped electrons to cross the turbulence eddies in the parallel and perpendicular directions. Because of the fast bounce motion, which averages out the parallel electric field, the trapped electrons cannot decorrelate from the wave in the parallel direction, i.e., $\tau_\parallel=\infty$. In the spectral range of interest, the CTEM frequency is roughly proportional to the toroidal mode number (i.e., nondispersive). Thus the resonant electrons cannot decorrelate from the wave in the toroidal direction. Moreover, although the resonant electrons can decorrelate from the wave in the radial direction due to the radial dependence of the precessional frequency, this dependence is very weak (on the equilibrium spatial scale). Therefore, $\tau_\perp=\infty$. The trapped electrons thus remain resonant with the wave until the eddies disappear or the electrons jump from one eddy to another, i.e, the resonant electrons behave like fluid eddies in the transport process. On the contrary, the ions in the ITG turbulence can experience parallel decorrelation with $\tau_\parallel=1/\langle \Delta k_\parallel v_i\rangle=1.8L_n/v_i$, since the parallel spectral width can be measured in Fig. 6(b). The ions can also be scattered radially by the radial structure of the poloidal harmonics of the ballooning modes, $\tau_\perp=3/(4\chi_i s^2\langle\theta^2\rangle\langle k_\theta^2\rangle)=2.0L_n/v_i$.

The fluid time scales also include eddy turnover time $\tau_{\rm eddy}$, zonal flow shearing time τ_s, and eddy autocorrelation time $\tau_{\rm au}$. The eddy turnover time $\tau_{\rm eddy}=L_r/\langle \delta v_r\rangle$, describes how fast the eddy rotates due to the $E\times B$ drift without the zonal flow shearing. For microscopic eddies, $\tau_{\rm eddy}\approx 1.6L_n/v_i$ by using the mean microscopic eddy size calculated in Sec. III C. For mesoscale eddies, the eddy turnover time is much longer. Another fluid time scale relevant to the dynamics of the turbulence eddies is the zonal flow shearing time,

$$\tau_s=\left[\frac{L_r}{L_\varphi}\frac{\partial}{\partial r}\left(\frac{qV_E}{r}\right)\right]^{-1},$$

which is calculated to be $\tau_s\approx 0.66L_n/v_i$. As calculated in Sec. V, the eddy autocorrelation time is $\tau_{\rm au}\approx 11L_n/v_i$.

We list all the characteristic time scales in Table. I. Compared with $\tau_{\rm decor}$, the zonal flow shearing time τ_s and eddy turnover time $\tau_{\rm eddy}$ are the two closest time scales in the CTEM turbulence. This suggests that the decorrelation process should be mostly the eddy mixing regulated by the zonal flow. All the kinetic time scales are much larger than $\tau_{\rm decor}$, τ_s, and $\tau_{\rm eddy}$. Therefore, the electron heat transport in the CTEM turbulence is mainly a fluid process although the linear instability is driven by the kinetic process of the toroidal precessional resonance. The radially random distribution of the microscopic and mesoscale eddies enables the electrons to average out the local structure of the turbulence intensity. The Kubo number is useful concept for the fluid turbulence. It is found that CTEM turbulence has a large Kubo number with $K=\tau_{\rm auto}/\tau_{\rm eddy}\approx 7$ for the microscopic eddies, which could affect the transport scaling.[64] This number only sets up a upper limit for the Kubo number because there exist also mesoscale eddies. Since the mesoscale eddies would have a smaller K value, the quasilinear estimate of the effective decorrelation time $\tau_{\rm decor}$ may be relevant to the transport on the global scale, which is in the transitional regime between the small and large K value.

For comparison, the ion characteristic time scales in the ITG turbulence are also listed in Table. I. The kinetic time scales, such as $\tau_\parallel$ and $\tau_\perp$, are close to $\tau_{\rm decor}$. Therefore, the transport in the ITG turbulence is mainly a kinetic process with parallel decorrelation or perpendicular decorrelation by the radial structure of the poloidal harmonics of the ballooning modes.[34] The zonal flow time τ_s is also found to be close to $\tau_{\rm decor}$, which suggests the importance of the zonal flow regulation on the ITG turbulence. For this kinetic decorrelation case, the Kubo number can be redefined as $K=\tau_\parallel/\tau_{\rm eddy}$, which leads to $K=0.37<1$. In this small Kubo number limit, the quasilinear theory should be valid.[64]

In the CTEM simulation, the transition from the Bohm scaling to gyro-Bohm scaling is observed when increasing the device size and keeping other tokamak parameters fixed. The significant long tail of the radial correlation function in Fig. 8 confirms the existence of a large number of mesoscale eddies in Fig. 7. The resonant trapped electrons can be convected by the $E\times B$ drift across the mesoscale eddies. This mesoscale ballistic motion then drives the electron heat transport that contains a nondiffusive component on the mesoscale and smooth out the small radial structure of the turbulence intensity, as shown in Fig. 11(a). The mesoscale ballistic electron heat flux, together with the turbulence spreading,[6] leads to the deviation from the gyro-Bohm scaling for the small devices. The transition from gyro-Bohm scaling to Bohm scaling when the device size decreases, is also observed for ion heat transport in the ITG turbulence,[6] which is mainly due to turbulence spreading.[32]

V. DISCUSSION AND CONCLUSION

In this paper, we carried out the nonlinear CTEM simulation using the global gyrokinetic code GTC with low particle noise. Our simulation finds that zonal flow is important in saturating the CTEM instability. The importance is further confirmed by the characteristic time analysis in which the zonal flow shearing time τ_s and the eddy turnover time τ_{eddy} are very close to the effective decorrelation time τ_{decor} that characterizes the transport process. The CTEM turbulence zonal flow, unlike the ITG turbulence, has prominent components in the short wavelength range, $\langle k_r\rho_i\rangle \sim 0.7$. The GAM oscillation can be found on the outside of the radius, albeit the low frequency zonal flow still dominates the saturation process.

The turbulence properties found by our CTEM simulation is consistent with the ballooning mode theory. Even in the nonlinear regime, the CTEM turbulence still exhibits a prominent ballooning structure. We find that the perpendicular wavelength has a significant downshift to the longer wavelength during the nonlinear saturation. However, the parallel wavelength keeps roughly the same.

The two-point correlation function is calculated to derive the radial correlation function, which shows that the CTEM turbulence contains both microscopic scale eddies of about $5\rho_i$ and mesoscale eddies of several tens of ρ_i. This two-scale structure of the turbulence eddies persists in different device sizes. The two-time-two-point correlation function is calculated to find the autocorrelation time of the turbulence. Comparing to the ITG turbulence, the CTEM turbulence has a shorter microscopic eddy size and parallel wavelength. These detailed properties of the turbulence fluctuations can provide useful information for both theoretical studies and experimental validations.

We also investigated the nonlinear heat transport mechanism. It is found that in the CTEM turbulence, the ion heat transport tracks the local profile of the turbulence intensity, which suggests that the ion transport is driven by the local $E\times B$ drift intensity. However, the electron heat transport only tracks the global profile of the turbulence intensity instead of the local profile. This suggests that electron transport in the CTEM turbulence could be locally nondiffusive. In addition, the probability density function of the flux-surface-averaged electron heat flux demonstrates some nonlognormal features, which further confirms the nondiffusiveness of the electron heat transport. The characteristic time scale analysis for the trapped electrons shows that the fluid time scales are close to the effective decorrelation time while the kinetic time scales are much larger, which suggests that the electron transport in the CTEM turbulence is a fluid process where the trapped electrons move with the turbulence eddies as fluid elements. For example, the resonant trapped electrons can be convected by the $E\times B$ drift across the mesoscale eddies. This mesoscale ballistic motion then drives the electron heat transport that contains a nondiffusive component on the mesoscale and smooths out the small radial structure of the turbulence intensity. The electron transport in the CTEM turbulence is a 1D process with the decorrelation and transport processes both occurring in the radial direction. In addition, it is found that the Kubo number $K>1$. Due to the large Kubo number and nonlocal feature of the electron transport, the quasilinear theory may no longer be valid locally for the electron transport in the CTEM turbulence. The persistence of mesoscale eddies changes the gyro-Bohm scaling to the Bohm scaling since the correlation length is comparable to the device size for small devices. It is also likely for the turbulence spreading[32,65] to play a role in this gyro-Bohm to Bohm transition. The ballistic electron heat flux may also account for the residual electron heat transport experimentally observed inside the ITB.

On the contrary, the ion transport in the ITG turbulence is driven by the local turbulence intensity and the transport mechanism is found to be parallel decorrelation due to the guiding center parallel motion and the parallel and radial structure of the poloidal harmonics of the ballooning modes. It is interesting to note that, the ion transport in the ITG turbulence, even the electron transport in the electron temperature gradient (ETG) turbulence,[34] is a 2D process with the decorrelation process occurring in the parallel direction and the transport process occurring the radial direction. Therefore, the Kubo number from the fluid turbulence needs to be modified to be relevant to the ITG turbulence and ETG turbulence,[34] and it is found the modified Kubo number $K \ll 1$. In this limit, the quasilinear theory is suitable to describe the ion transport in the ITG and CTEM turbulence, as well as the electron transport in the ETG turbulence. In addition, the transition from gyro-Bohm to Bohm scaling in the ITG turbulence is mainly due to the turbulence spreading since no significant mesoscale eddies are observed.[32]

ACKNOWLEDGMENTS

This work was supported by U.S. DOE SciDAC GPS-TTBP and GSEP centers. Simulations used ORNL and NERSC supercomputers.

We acknowledge L. Chen, P. H. Diamond, and T. S. Hahm for useful discussions.

[1] W. Horton, Rev. Mod. Phys. **71**, 735 (1999).
[2] Z. Lin, T. Hahm, W. Lee, W. Tang, and R. White, Science **281**, 1835 (1998).
[3] T. Hahm and K. Burrell, Phys. Plasmas **2**, 1648 (1995).
[4] M. Beer, Ph.D. thesis, Princeton University, 1995.
[5] H. Biglari, P. Diamond, and P. Terry, Phys. Fluids B **2**, 1 (1990).
[6] Z. Lin, S. Ethier, T. Hahm, and W. Tang, Phys. Rev. Lett. **88**, 195004 (2002).
[7] For more information, see http://www.iter.org.
[8] B. Kadomstev and O. Pogutse, Sov. Phys. Dokl. **14**, 470 (1969).
[9] J. Adam, W. Tang, and P. Rutherford, Phys. Fluids **19**, 561 (1976).
[10] B. Coppi and G. Rewoldt, Phys. Rev. Lett. **33**, 1329 (1974).
[11] P. Catto and K. Tsang, Phys. Fluids **21**, 1381 (1978).
[12] W. Tang, Nucl. Fusion **18**, 1089 (1978).
[13] L. Chen, R. L. Berger, J. G. Lominadze, M. N. Rosenbluth, and P. H. Rutherford, Phys. Rev. Lett. **39**, 754 (1977).
[14] T. S. Hahm and W. M. Tang, Phys. Fluids B **3**, 989 (1991).
[15] P. W. Terry, Phys. Rev. Lett. **93**, 235004 (2004).
[16] P. Catto, W. Tang, and D. Baldwin, Plasma Phys. **23**, 639 (1981).

[17]E. Frieman and L. Chen, Phys. Fluids **25**, 502 (1982).
[18]W. Lee, Phys. Fluids **26**, 556 (1983).
[19]W. Lee, J. Comput. Phys. **72**, 243 (1987).
[20]A. Dimits and W. Lee, J. Comput. Phys. **107**, 309 (1993).
[21]S. E. Parker and W. W. Lee, Phys. Fluids B **5**, 77 (1993).
[22]R. D. Sydora, V. K. Decyk, and J. M. Dawson, Plasma Phys. Controlled Fusion **38**, A281 (1996).
[23]M. Kotschenreuther, G. Rewoldt, and W. Tang, Comput. Phys. Commun. **88**, 128 (1995).
[24]A. M. Dimits, G. Bateman, M. A. Beer, B. I. Cohen, W. Dorland, G. W. Hammett, C. Kim, J. E. Kinsey, M. Kotschenreuther, A. H. Kritz, L. L. Lao, J. Mandrekas, W. M. Nevins, S. E. Parker, A. J. Redd, D. E. Shumaker, R. Sydora, and J. Weiland, Phys. Plasmas **7**, 969 (2000).
[25]L. Chen, Z. Lin, and R. White, Phys. Plasmas **7**, 3129 (2000).
[26]P. Diamond, S.-I. Itoh, K. Itoh, and T. Hahm, Plasma Phys. Controlled Fusion **47**, R35 (2005).
[27]D. R. Ernst, P. T. Bonoli, P. J. Catto, W. Dorland, C. L. Fiore, R. S. Granetz, M. Greenwald, A. E. Hubbard, M. Porkolab, M. H. Redi, J. E. Rice, K. Zhurovich, and Alcator C-Mod Group, Phys. Plasmas **11**, 2637 (2004).
[28]F. Merz and F. Jenko, Phys. Rev. Lett. **100**, 035005 (2008).
[29]J. Lang, S. Parker, and Y. Chen, Phys. Plasmas **15**, 055907 (2008).
[30]D. Ernst, J. Lang, W. Nevins, M. Hoffman, Y. Chen, W. Dorland, and S. Parker, Phys. Plasmas **16**, 055906 (2009).
[31]R. Waltz and C. Holland, Phys. Plasmas **15**, 122503 (2008).
[32]Z. Lin and T. Hahm, Phys. Plasmas **11**, 1099 (2004).
[33]L. Lin, M. Porkolab, E. M. Edlund, J. C. Rost, M. Greenwald, N. Tsujii, J. Candy, R. E. Waltz, and D. R. Mikkelsen, Plasma Phys. Controlled Fusion **51**, 065006 (2009).
[34]Z. Lin, I. Holod, L. Chen, P. H. Diamond, T. S. Hahm, and S. Ethier, Phys. Rev. Lett. **99**, 265003 (2007).
[35]Y. Xiao and Z. Lin, Phys. Rev. Lett. **103**, 085004 (2009).
[36]M. E. Austin, K. H. Burrell, R. E. Waltz, K. W. Gentle, P. Gohil, C. M. Greenfield, R. J. Groebner, W. W. Heidbrink, Y. Luo, J. E. Kinsey, M. A. Makowski, G. R. McKee, R. Nazikian, C. C. Petty, R. Prater, T. L. Rhodes, M. W. Shafer, and M. A. V. Zeeland, Phys. Plasmas **13**, 082502 (2006).
[37]Z. Lin and W. Lee, Phys. Rev. E **52**, 5646 (1995).
[38]Z. Lin and L. Chen, Phys. Plasmas **8**, 1447 (2001).
[39]Z. Lin, Y. Nishimura, Y. Xiao, I. Holod, W. Zhang, and L. Chen, Plasma Phys. Controlled Fusion **49**, B163 (2007).
[40]Y. Xiao, P. J. Catto, and W. Dorland, Phys. Plasmas **14**, 055910 (2007).
[41]J. Lofstead, F. Zheng, S. Klasky, and K. Schwan, Proceedings of the 24th International Parallel and Distributed Processing Symposium, Rome, 2009 (unpublished).
[42]G. Rewoldt, Z. Lin, and Y. Idomura, Comput. Phys. Commun. **177**, 775 (2007).
[43]A. Aydemir, Phys. Plasmas **1**, 822 (1994).
[44]A. Bottino, Phys. Plasmas **14**, 010701 (2007).
[45]I. Holod and Z. Lin, Phys. Plasmas **14**, 032306 (2007).
[46]L. Wang and T. S. Hahm, Phys. Plasmas **16**, 062309 (2009).
[47]G. Kagan and P. J. Catto, Plasma Phys. Controlled Fusion **50**, 085010 (2008).
[48]Y. Xiao and P. Catto, Phys. Plasmas **13**, 102311 (2006).
[49]F. Jenko, W. Dorland, M. Kotschenreuther, and B. Rogers, Phys. Plasmas **7**, 1904 (2000).
[50]T. Hahm, M. Beer, Z. Lin, G. Hammett, W. Lee, and W. Tang, Phys. Plasmas **6**, 922 (1999).
[51]F. I. Parra and P. J. Catto, Plasma Phys. Controlled Fusion **51**, 065002 (2009).
[52]F. I. Parra and P. J. Catto, Plasma Phys. Controlled Fusion **50**, 065014 (2008).
[53]W. W. Lee and R. A. Kolesnikov, Phys. Plasmas **16**, 044506 (2009).
[54]Z. Gao, K. Itoh, H. Sanuki, and J. Dong, Phys. Plasmas **13**, 100702 (2006).
[55]T. Watari, Y. Hamada, T. Notake, N. Takeuchi, and K. Itoh, Phys. Plasmas **13**, 062504 (2006).
[56]X. Xu, Z. Xiong, Z. Gao, W. Nevins, and G. Mckee, Phys. Rev. Lett. **100**, 215001 (2008).
[57]V. Naulin, A. Kendl, O. E. Garcia, A. H. Nielsen, and J. J. Rasmussen, Phys. Plasmas **12**, 052515 (2005).
[58]J. W. Connor, R. J. Hastie, and J. B. Taylor, Phys. Rev. Lett. **40**, 396 (1978).
[59]J. DeBoo, S. Cirant, T. Luce, A. Manini, C. Petty, F. Ryter, M. Austin, D. Baker, K. Gentle, C. Greenfield, J. Kinsey, and G. Staebler, Nucl. Fusion **45**, 494 (2005).
[60]F. Ryter, C. Angioni, A. G. Peeters, F. Leuterer, H.-U. Fahrbach, and W. Suttrop, Phys. Rev. Lett. **95**, 085001 (2005).
[61]I. Holod and Z. Lin, Phys. Plasmas **15**, 092302 (2008).
[62]W. Zhang, Z. Lin, and L. Chen, Phys. Rev. Lett. **101**, 095001 (2008).
[63]R. Basu, T. Jessen, V. Naulin, and J. Rasmussen, Phys. Plasmas **10**, 2696 (2003).
[64]M. Vlad, F. Spineanu, J. Misguich, J.-D. Reuss, R. Balescu, K. Itoh, and S.-I. Itoh, Plasma Phys. Controlled Fusion **46**, 1051 (2004).
[65]W. Deng and Z. Lin, Phys. Plasmas **16**, 102503 (2009).